Land cover mapping from orthorectified Neo-Pleiades imagery via Object-Based methods

Valerio Baiocchi [1], Francesca Giannone [2], Chiara Magurano [1]
Erica Nocerino [3]
[1] DICEA Sapienza, Rome, Italy – valerio.baiocchi@uniroma1.it – chiara.magurano@uniroma1.it
[2] Departement of Civil Engineering, Niccolò Cusano University, Rome, Italy – francesca.giannone@unicusano.it
[3] DUMAS University of Sassari, Sassari, Italy – enocerino@uniss.it

Keywords: Neo-Pleiades, Posidonia Oceanica, Sardinia, Orthorectification, Object Based, Golfo Aranci

Abstract

Posidonia oceanica is one of the most important seagrass species in the Mediterranean Sea, providing essential ecosystem services such as carbon sequestration, coastal protection and acting as a habitat and nursery ground for numerous marine species. These meadows have experienced significant decline in recent decades due to increasing anthropogenic pressures and environmental changes. Accurate and efficient mapping techniques are therefore essential for monitoring their spatial distribution and supporting conservation efforts. This study investigates the potential of very high-resolution Neo-Pléiades satellite imagery for mapping *P. oceanica* meadows along the northeastern coast of Sardinia (Italy). Two satellite acquisitions from 2021 and 2022 were orthorectified in PCI Catalyst (v.2023.0.0) using a Rational Polynomial Coefficient (RPC) model. Subsequently, a water column correction based on the Lyzenga depth-invariant index was applied to reduce depth-related spectral variability. The images were then classified using an object-based image analysis approach implemented in eCognition Developer (v.10.5), comparing three supervised algorithms: Nearest Neighbor (NN), Support Vector Machines (SVM), and Random Tree (RT). Accuracy assessment based on confusion matrices showed high classification performance, with overall accuracies up to 0.97 and Kappa values up to 0.96. Additional spatial validation using manually delineated reference areas confirmed classification reliability, although slightly lower agreement values were observed compared to confusion matrix estimates. The results highlight the strong potential of integrating high-resolution satellite imagery, water column correction, and object-based classification for mapping and monitoring *P. oceanica* habitats.

1. Introduction

Posidonia oceanica (Linnaeus) Delile (hereafter referred to as PO) represents one of the most ecologically important marine phanerogams. PO is endemic to the Mediterranean Sea, occurring from Gibraltar to Turkey, and from North African shores to the Adriatic. In Italy, it is widespread in both the Tyrrhenian and Adriatic Seas and surrounds the islands of Sicily and Sardinia. As a flowering plant, it performs photosynthesis and possesses a well-developed system of roots, leaves, and fruits. Because of its need to photosynthesize, its occurrence is not uniform. Its meadows develop under specific environmental conditions characterized by high water clarity, stable salinity, and sufficient light penetration, colonizing continental shelves down to depths of approximately 40 m, covering roughly 2% of the seafloor. In highly oligotrophic waters, they can extend down to 50 meters (Cocozza et al., 2024). Optimal growth occurs around 20°C, while elevated water temperatures, especially during marine heatwaves, can reduce oxygen levels, negatively affecting meadow vitality. Human pressures such as pollution, urban expansion, and maritime traffic have led to a marked decline and fragmentation of these meadows, reducing their capacity to recover and persist in some areas.

Human impacts on marine environments are therefore central to understanding the threats this species faces. Over the last five decades, PO populations have declined by about 34%, with losses reaching 56% in the northwestern Mediterranean (Robello et al., 2024). PO is a key component of coastal ecosystems; therefore, the decline of its meadows has significant environmental and socio-economic implications. Understanding its biology, ecology, geographic distribution, associated threats, and the importance of its conservation is therefore essential.

From an ecological perspective, PO meadows perform multiple ecosystem functions that extend well beyond their role as habitat for marine organisms. They improve water quality by absorbing nutrients and, most notably, act as major blue carbon sinks, storing carbon dioxide in seabed sediments and thereby helping to mitigate climate change (Trevathan-Tackett et al., 2015). They also play a protective role by stabilizing sediments and buffering coastlines against wave-induced erosion.

Given these circumstances, monitoring PO and improving the efficiency of mapping methodologies has become a major focus of current research. A wide range of techniques has been developed to map these underwater habitats, from traditional approaches such as aerial photography, side-scan sonar, and multibeam echosounders to more recent remote sensing technologies. More recently, optical remote sensing technologies, based on satellite, aerial, and UAV imagery (Ventura et al., 2018), have gained prominence. These approaches are often combined with laser-based techniques like LiDAR to incorporate bathymetric information (Panagou et al., 2020). These methodologies support a range of analyses, including coastline extraction (Alcaras et al., 2021), the monitoring of seagrass dynamics, the assessment of temporal changes, and the estimation of meadow extent and coverage. The chosen workflow for these types of studies depends on the type of sensor and the data level provided by the supplier, as products may vary in their degree of preprocessing. For example, the study by (Chowdhury et al., 2024) analyzed Sentinel-1 and Sentinel-2 data from surveys conducted in 2021 over the Balearic and Maltese Islands to map PO meadows. Alternatively, (Yfantidou et al., 2019) employed images from the Landsat 8 constellation to achieve the same objective.

In this study, two Neo-Pléiades images, covering the eastern coast of Sardinia (Italy) were acquired. Orthorectification was performed using the Rational Polynomial Coefficient (RPC) model, supported by Ground Control Points (GCPs) and Check Points (CPs) to assess precision and accuracy. In this case, orthorectification also targeted the submerged portions of the imagery, where two major challenges arise: the limited availability of GCPs and the complexity of correcting for geometric distortions caused by water depth. Subsequently, a water column correction algorithm was applied to minimize water column effects and improve seabed signal retrieval. The paper concludes with preliminary results of an object-based classification experiment on PO meadows, comparing three different classification approaches: Nearest Neighbor (NN), Support Vector Machines (SVM) and Random Tree (RT). The workflow of this research is shown in Figure 1.

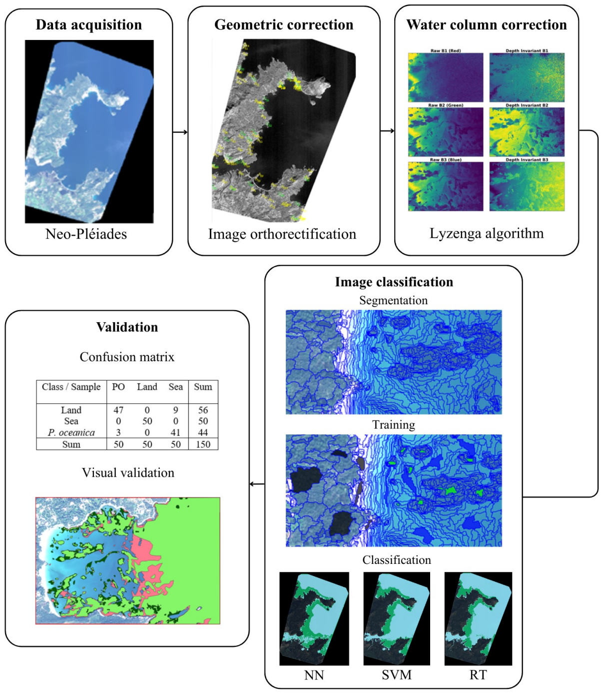

Figure 1. General workflow of the study presented in this paper.

2. Materials and Methods

2.1 Study area

This paper focuses on the orthorectification and classification of satellite imagery acquired by the Neo-Pléiades satellite constellation. The two raw acquisitions used were captured on 27/11/2021 at 10:15 GMT and 02/01/2022 at 10:33 GMT. They cover a portion of the northeastern coast of Sardinia, specifically between Golfo Aranci and Capo Ceraso (Figure 2).
In Sardinian coastal landscapes, granitic lithologies are common (Cammarano et al., 2025), and coastal waters are often relatively clear. However, local variations in turbidity, for instance due to river discharge or sediment resuspension, can still affect the visibility of submerged habitats.

2.2 Satellite data

Launched in 2021, the Neo-Pléiades constellation operates in a sun-synchronous, near-polar low Earth orbit at an altitude of 620 km, allowing the satellites to maintain consistent illumination conditions, revisit the same point twice per day, and achieve near-global coverage. The Neo-Pléiades sensors provide very high-resolution data, with 30 cm for the panchromatic band and 1.2 m for multispectral bands.

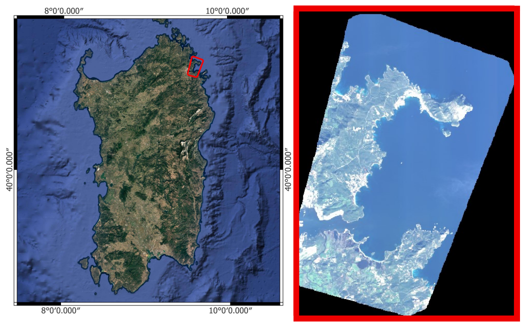

Figure 2. Geographical location of the study area. The left panel depicts the location of the island of Sardinia (EPSG: 4326), while the right panel indicates the location of the area covered by the Neo-Pléiades images, between Golfo Aranci and Capo Ceraso.

Each satellite has a 14 km swath width, a 26-day repetition cycle, and an expected operational lifetime of ten years. The bands on which the constellation operates are seven in total (Table 1).

Band	Wavelength Range (nm)
Panchromatic	450–800
Deep blue	400–450
Blue	450–520
Green	530–590
Red	620–690
Red edge	700–750
Near infrared	770–880

Table 1. Neo-Pléiades operational bands and corresponding wavelengths range.

2.3 Methodology

To support geometric correction, additional datasets were obtained from the Sardinia Region’s official geoportal, including a 1 m resolution LiDAR-derived Digital Terrain Model (DTM) and a 1:2000 Regional Technical Map (CTR). Since no high-resolution open-access bathymetric model was available, depth contours were digitized from nautical charts produced by the Italian Hydrographic Institute (garmin.com/it-

IT/c/marine-cartography/third-party-marine-maps/), enabling the integration of terrestrial and marine elevation data into a continuous model. The charts refer to the Lower Astronomical Tide (L.A.T.) and not orthometric height.

Approximately one hundred GCPs and CPs were extracted in QGIS (v.3.28) from LiDAR data and high-precision cartography. Orthorectification was performed in PCI Catalyst (v.2023.0.0) using a Rational Polynomial Coefficient model (Figure 3).

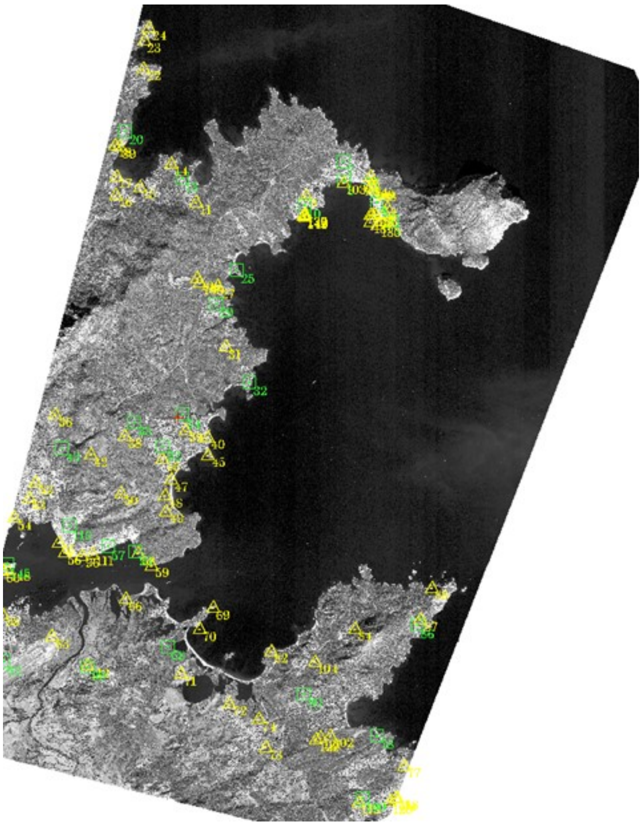

Figure 3. View of the 2021 Panchromatic image in PCI Catalyst. Ground Control Points are shown in yellow, and Check Points in green.

The workflow first involved orthorectifying the panchromatic images. The multispectral images were pansharpened and subsequently orthorectified using the same GCP and CP network. For the original multispectral images, a coordinate conversion was applied to ensure consistency with the pansharpened products (Baiocchi et al., 2025).

The orthorectified multispectral images were then subjected to water column correction, using the DII algorithm by Lyzenga (Lyzenga, 1978). The correction relies on the assumption that light intensity decreases exponentially with increasing depth as it travels through the water column. To reduce this depth-related effect, spectral values from the visible bands are extracted from the same substrate type observed at different depths. These values are then used to estimate the attenuation of light in the water column in order to reduce the influence of water depth on the spectral signal and enhance the discrimination of seabed substrates.

A homogeneous seabed area was selected to estimate light attenuation within the water column using spectral values from the visible bands together with bathymetric data. After correcting for deep-water radiance and applying a logarithmic transformation, attenuation coefficients were estimated through linear regression. These coefficients were then used to compute depth-invariant indices, generating new spectral bands that reduce the influence of water depth and enhance seabed discrimination. The resulting bands were subsequently normalized, interpolated to remove missing values within the water mask, and smoothed before being exported for object-based image analysis (Figure 4).

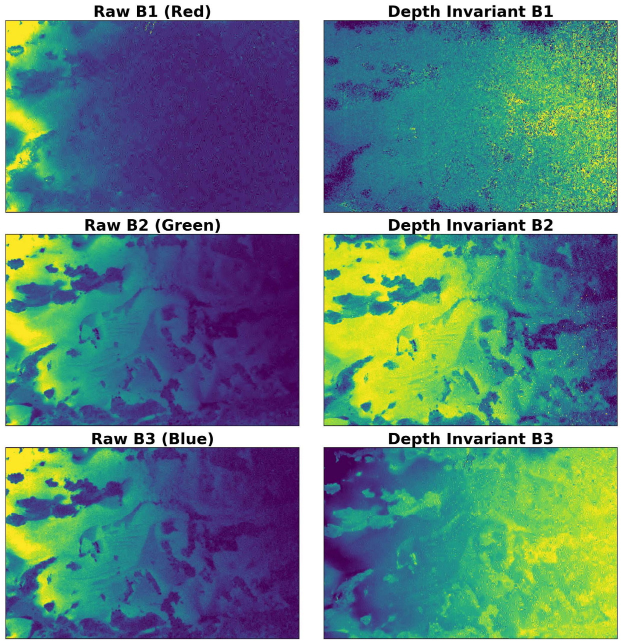

Figure 4. Comparison between the original RGB spectral bands and the respective depth-invariant bands obtained after water column correction on a small test area. The correction reduces the influence of water depth on the spectral signal, making seabed features more visible across different depths. Colours are displayed using a colour scale for visualization purposes and do not correspond to the true spectral colours of the bands.

The resulting datasets were then imported into eCognition Developer (v.10.5) for object-based image analysis. The segmentation process began with multiresolution segmentation, during which the scale, shape, and compactness parameters were adjusted to generate polygonal objects with an average size of approximately 50 m, reflecting both the coastal geomorphology and the spectral variability of the image (Figure 5).

The shape parameter was set to 0.5 and compactness to 0.6. This configuration ensured a balanced contribution between spectral information and object geometry, allowing the segmentation to follow spectral heterogeneity while avoiding the creation of excessively compact or elongated objects.
A supervised classification was then performed using three different classification methods (NN, SVM and RT), selected due to their reliability, computational efficiency, and widespread use in object-based environmental mapping applications (Rende et al., 2020; Rende et al., 2022 and Zaaboub et al., 2023).

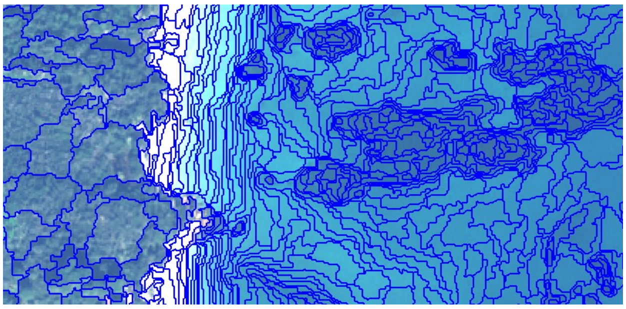

Figure 5. Multiresolution segmentation performed in *eCognition Developer* (v.10.5).

Approximately 100 training objects were manually selected for each of the three target classes (Figure 6) and were used to train the three algorithms, which subsequently generated the classified maps.

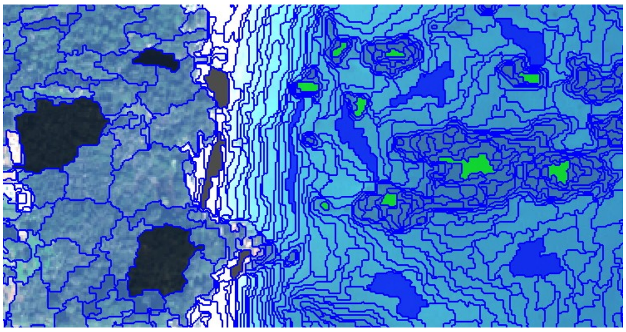

Figure 6. Example of training polygons in eCognition Developer (v.10.5) visually chosen and then manually selected to train the algorithm to recognize the three main classes: Land (in black), *Posidonia oceanica* (in green) and Sea (in blue).

The NN classifier works by comparing each object with reference objects and assigning it to the class of the most similar, or “nearest”, reference in terms of spectral and spatial characteristics (Zaaboub et al., 2023).
The SVM classifier constructs a hyperplane or set of hyperplanes in a high-dimensional space to separate different classes. The optimal hyperplane maximizes the distance (margin) to the nearest training objects of any class, which generally improves the classifier’s generalization ability (Boser et al., 1992).
The RT algorithm builds multiple decision trees using random subsets of objects and features. Each tree predicts independently, and the final classification is determined by majority vote, which improves accuracy and reduces overfitting (Makri et al., 2025).

3. Results and Discussion

For each of the two years (2021 and 2022), the multispectral, panchromatic, and pansharpened images were orthorectified both with and without bathymetric correction, resulting in a total of 12 orthorectified satellite images.

The process employed approximately 80 GCPs and 20 CPs. Orthorectification accuracy was assessed through the analysis of CPs. The average CP residuals ranged between 30 and 40 cm, slightly higher than those of the GCPs (25–30 cm), as expected since CPs are used for independent validation (Table 2). These errors fall within an acceptable tolerance considering the 30 cm spatial resolution of the panchromatic images, indicating that the correction model is consistent with the nominal resolution of the sensor across both panchromatic and multispectral products.

A well-recognized systematic discrepancy exists between the residuals in the North and East directions. In particular, the E (East) coordinate generally shows higher accuracy than the N (North) coordinate. This difference stems from the satellite’s pushbroom acquisition technique, where the sensor records a full swath of terrain at once along the direction perpendicular to the satellite’s motion. As a result, the East coordinate is captured across the satellite’s flight path, making it more stable and geometrically “rigid,” and therefore less sensitive to temporal variations.

Conversely, the North coordinate is affected by the satellite’s forward motion along its orbit, as well as by the stability of the platform and its navigation systems during data acquisition. Because the image is formed progressively as the satellite moves, even small instabilities in flight or data recording can introduce greater uncertainty in this direction.

2021 Multispectral Image (Ground Units)			
	E RMS	N RMS	H RMS
GCP	0.268	0.242	0.097
CP	0.363	0.463	0.184

2022 Multispectral Image (Ground Units)			
	E RMS	N RMS	H RMS
GCP	0.24	0.277	0.13
CP	0.335	0.462	0.179

2021 Pansharpened Image (Ground Units)			
	E RMS	N RMS	H RMS
GCP	0.272	0.245	0.098
CP	0.362	0.462	0.184

2022 Pansharpened Image (Ground Units)			
	E RMS	N RMS	H RMS
GCP	0.244	0.281	0.132
CP	0.335	0.461	0.179

Table 2. Total residual errors for the multispectral and the pansharpened images expressed in ground units (meters).

Regarding orthorectification accuracy, it is currently not possible to precisely quantify this effect, since the ground control points (GCPs) and check points (CPs) used were measured on land, and no accurately surveyed control points exist on the seafloor. Furthermore, the positional accuracy of the GCPs and CPs is inherently constrained by the source cartography, which was available at a scale of 1:2000. Based on standard cartographic accuracy assumptions, this corresponds to an expected planimetric accuracy of approximately 0.4 m and a vertical accuracy of about 0.6–0.7 m. In the context of satellite imagery, it is generally expected that geometric accuracy should be on the order of the ground sample distance (GSD), or approximately half a pixel. The obtained residuals for the CPs are generally consistent with the expected accuracy of the imagery, being on the order of the GSD. Slightly higher errors observed in the N coordinate remain acceptable and are consistent with both the pushbroom acquisition geometry and the scale of the reference cartography.

Lastly, the influence of bathymetry is evident through noticeable differences in the shape and position of the seabed and, consequently, in the distribution of PO meadows. This demonstrates that the effect of seafloor depth cannot be overlooked (Figure 7).

Figure 7. Orthorectified 2021 pansharpened image after bathymetric correction. Bathymetric correction alters the apparent shape and position of the seabed and PO meadows. Red polygons indicate two PO patches manually delineated before correction, while blue polygons show the same patches after bathymetric correction.

Following orthorectification, the multispectral images from 2021 and 2022, along with the DII index corrected bands, were imported into eCognition Developer (v.10.5) to perform an object-based classification with three different classifiers supplied by the software (NN, SVM and RT). Image segmentation was applied using scale, shape, and compactness parameters optimized for the coastal landscape, generating objects that captured both geomorphological structure and spectral variability. Three classes were considered: Land, Sea, and *Posidonia oceanica*. For each class, approximately 100 representative objects were manually selected as training samples, and an additional set of roughly 50 objects per class was used for independent accuracy assessment. The computation time was approximately 20 minutes for the SVM and RT classifiers, and around 40 minutes for the NN classifier, although these values may vary depending on the computational performance of the hardware used. In the case of this study, the processor used was an AMD Ryzen 9 3900X 12-Core Processor (4.00 GHz), with a RAM of 128 GB.
The resulting six thematic maps, as seen for example in Figure 8 and Figure 9, show a clear delineation of PO meadows along the northeastern Sardinian coast.
Visual inspection revealed a few zones where PO was detected in areas that appeared optically deep or unclear. However, considering that this species can grow at depths up to 50 m, corresponding to the maximum depth represented in the bathymetric model, these detections cannot be completely dismissed as classification errors.

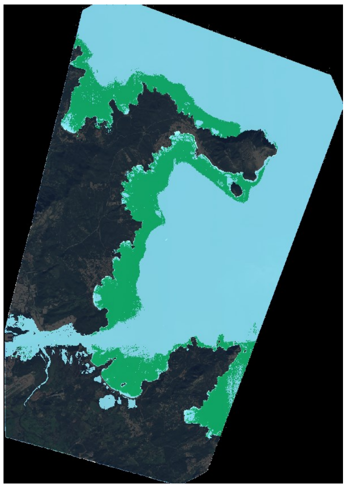

Figure 8. Classified 2021 Neo-Pléiades multispectral image, through the SVM algorithm. Land is shown in black, sea in light blue, and *Posidonia oceanica* in green.

Another aspect that can be observed through visual inspection is that, in some classifications, inland waters are not accurately classified (see Figure 9 as an example).

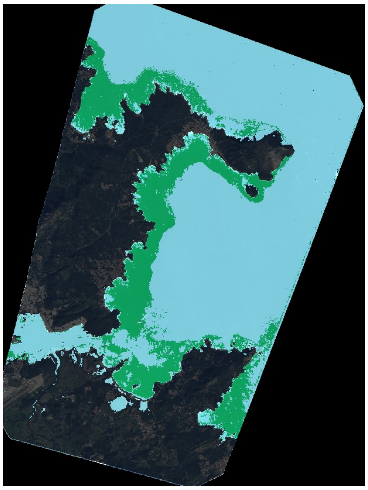

Figure 9. Classified 2022 Neo-Pléiades multispectral image, through the SVM algorithm. Land is shown in black, sea in light blue, and *Posidonia oceanica* in green.

Quantitative assessment of the classification accuracy of the three classification methods was conducted through confusion matrices, as shown for example in Table 3.

Class / Sample	PO	Land	Sea	Sum
Land	47	0	9	56
Sea	0	50	0	50
PO	3	0	41	44
Sum	50	50	50	150

Table 3. Confusion matrix resulting from the classification of the 2021 multispectral image with the RT algorithm.

The overall accuracy of the classifications, according to the confusion matrices, has produced very high results for both years (Table 4 and 5).

Classifier	OA	Kappa	Producer (PO)	User (PO)
NN	0.97	0.96	0.97	0.95
SVM	0.94	0.91	0.91	0.95
RT	0.92	0.88	0.94	0.89

Table 4. Accuracy assessment for the three classifications performed on the 2021 multispectral image. The reported metrics include Overall Accuracy (OA), the Kappa coefficient, Producer Accuracy for the PO class, and User Accuracy for the PO class.

Classifier	OA	Kappa	Producer (PO)	User (PO)
NN	0.95	0.92	0.93	0.95
SVM	0.92	0.88	0.86	0.98
RT	0.74	0.60	0.68	0.75

Table 5. Accuracy assessment for the three classifications performed on the 2022 multispectral image. The reported metrics include Overall Accuracy (OA), the Kappa coefficient, Producer Accuracy for the PO class, and User Accuracy for the PO class.

Overall, the Land class showed nearly perfect agreement in all years. Minor confusion was observed between Sea and PO, mainly attributable to spectral similarities in shallow coastal waters, where water column effects and seabed reflectance transitions are strongest.

Although the obtained classification accuracies are high, some limitations must be considered when interpreting these results. Firstly, the training samples used for the classification methods were derived solely through visual inspection of the imagery, without the support of *in situ* observations, which are commonly incorporated in other studies (Giménez-Romero et al., 2025; Roca et al., 2025; Traganos et al., 2022). This approach is common in preliminary remote sensing studies, but it may lead to ambiguities in areas where spectral signatures of PO and surrounding substrates overlap. For this reason, integrating field data would significantly improve the reliability of both the training and validation datasets and reduce classification uncertainty.

As a complementary validation approach, three test areas were selected within the satellite imagery. Within these areas, the boundaries of the PO meadows were manually delineated in QGIS (v.3.28) based on visual interpretation. The selected areas were located in shallow waters, where the seabed and meadow limits were clearly visible in the imagery. The classification results obtained from the different algorithms were then overlaid with these reference polygons in order to perform a spatial comparison between the mapped and manually delineated meadow boundaries. This approach allowed a more detailed assessment of the spatial accuracy of the classifications. As illustrated in Figure 10, the extent of PO coverage produced by the algorithms does not always perfectly match the manually delineated boundaries, revealing discrepancies that are not fully captured by the confusion matrices.

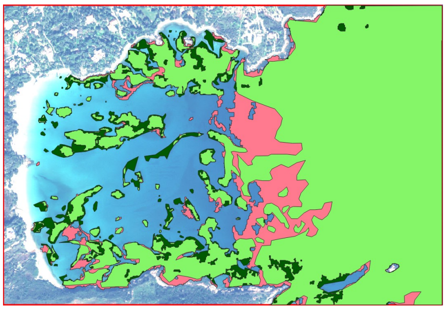

Figure 10. Coverage comparison between the NN classification (2021 image) and the manually delineated *Posidonia oceanica* meadow in one of the selected validation areas. Bright green indicates areas of agreement between the manual delineation and the NN classification. Red highlights areas incorrectly classified as PO by the NN algorithm, while dark green represents PO areas identified during manual delineation but not detected by the classifier.

By calculating the respective areas, it is possible to estimate the proportion of correctly classified PO coverage within the selected validation areas, using the manually delineated polygons as reference. In the case reported in Table 6, for example, the NN algorithm applied to the 2021 image correctly identified approximately 91% of the PO area that had been manually delineated by the authors. Although this still represents a high level of agreement, it is slightly lower than the accuracy values obtained from the confusion matrices.

Classifier	Area (m^2)
NN	540852
QGIS	514699
Correct	468057

Table 6. Calculation of the PO coverage estimated by the NN classifier within one of the selected validation areas for the 2021 image. The table reports the area classified as PO by the NN algorithm, the area manually delineated in QGIS, and the overlap between the two, representing the correctly classified area.

CL	Test area (n)	Area from classification (m^2)	Area from QGIS (m^2)	Correctly classified (m^2)	Accuracy (%)
NN	1	540852	514699	468057	91
	2	2347828	2251796	2195633	98
	3	813403	800038	731474	91
SVM	1	484302	514699	431560	83
	2	2254295	2251796	2144232	95
	3	678282	800038	653584	95
RT	1	585655	514699	471938	92
	2	2421819	2251796	2177637	97
	3	797923	800038	724195	91

Table 7. Calculation of the PO coverage estimated by the algorithms within the selected validation areas for the 2021 image. The table reports the type of algorithm, the area classified as PO by the algorithms, the area manually delineated in QGIS, the overlap between the two and the accuracy in that specific area.

https://doi.org/10.5194/isprs-archives-XLIX-B3-2026-701-2026

The same principle can be applied to the rest of the classifiers, as seen in Table 7 for the 2021 image and in Table 8 for the 2022 image.

CL	Test area (n)	Area from classification (m^2)	Area from QGIS (m^2)	Correctly classified (m^2)	Accuracy (%)
NN	1	517540	491696	434171	88
	2	2182643	2253253	2029121	90
	3	734135	775377	649028	84
SVM	1	411584	491696	354167	72
	2	2135114	2253253	2021853	90
	3	637189	775377	582208	75
RT	1	677422	491696	443722	90
	2	2423580	2253253	2163068	96
	3	731146	775377	570014	74

Table 8. Calculation of the PO coverage estimated by the algorithms within the selected validation areas for the 2022 image.

The results from the second validation method show that the overall accuracy of the classification methods is still high, but consistently lower than what the confusion matrices may have indicated (Table 9).

CL	Year	OA from confusion matrices (%)	OA from visual validation (%)
NN	2021	97	93
SVM	2021	94	91
RT	2021	92	93
NN	2022	95	87
SVM	2022	92	79
RT	2022	74	87

Table 9. Comparison between the overall accuracies perceived by the confusion matrices for the three algorithms for each year and the overall accuracies calculated from visual validation.

Another limitation of this study concerns the quality of the bathymetric data. Depth contours were digitized from nautical charts produced by the Italian Hydrographic Institute (IIM), as no open-source bathymetric datasets with a spatial resolution comparable to the satellite imagery were available. Following interpolation performed in PCI Catalyst (v.2023.0.0), the resulting bathymetric model had a spatial resolution of 10 m.

Although this represents a limitation, the objective of this study is to highlight the importance of bathymetric correction within the methodological workflow. The availability of higher-resolution bathymetric data would likely improve the performance of the water column correction and, consequently, the accuracy of the classification results.

Another limitation concerns environmental factors such as water clarity. Light penetration in the water column is limited, and therefore the deeper boundary of PO meadows may not be detectable in satellite imagery. Water turbidity, often related to suspended sediments, can significantly reduce light penetration. In Sardinian coastal environments such as the one in this study, where granitic lithologies are common, coastal waters are often relatively clear; however, local variations in turbidity can still affect the visibility of submerged habitats.

Lastly, while the algorithms used provided robust and consistent results, they represent only three of the many supervised object-based approaches available in the literature. Since no standardized classification workflow currently exists for PO detection in very high-resolution imagery, future studies should compare a wider range of algorithms to better understand their respective strengths and limitations. Such comparisons would help identify the most suitable strategies under varying environmental and radiometric conditions, contributing to the development of a more generalizable methodological framework.

4. Conclusions

This study demonstrates that very high-resolution Neo-Pléiades imagery, combined with object-based image analysis and supervised classification methods, can effectively delineate *Posidonia oceanica* meadows along the northeastern coast of Sardinia. The proposed workflow integrates geometric correction, water column correction using the Lyzenga depth-invariant index, and object-based classification approaches, enabling the extraction of seabed information from optical satellite imagery.

The classification experiments performed on the 2021 and 2022 acquisitions produced high accuracy levels for most algorithms. The Nearest Neighbor classifier achieved the highest performance, with overall accuracies exceeding 95% and Kappa values above 0.90, while Support Vector Machines (SVM) also produced consistently reliable results. The Random Tree (RT) classifier showed slightly lower performance, particularly for the 2022 dataset, highlighting how classification accuracy may vary depending on environmental conditions and image characteristics.

A second validation approach, based on the spatial comparison between the classified maps and manually delineated PO meadow boundaries within selected test areas, provided a complementary assessment of the results. This analysis revealed that the effective spatial agreement between classifications and reference polygons was generally slightly lower than the accuracies derived from the confusion matrices. These findings suggest that confusion matrix metrics alone may partially overestimate classification performance, while spatial validation allows to get closer to a more realistic evaluation of the correspondence between mapped and actual meadow extents.

The results also emphasize the importance of water column correction for improving seabed discrimination. By reducing the influence of depth on the spectral signal, the depth-invariant indices allowed clearer identification of benthic substrates and improved the separability between PO meadows and surrounding seabed classes.

Despite the promising results, several limitations must be considered. Training samples were derived through visual interpretation and were used as reference data, but they cannot be considered a true ground truth, as they were derived from the same imagery used for classification. Therefore, their accuracy is inherently dependent on the interpreter’s expertise and on image quality, and can be assumed to be high in optically clear and shallow areas but lower in deeper or more ambiguous zones. For this reason, the reported agreement values should be interpreted as an indication of relative spatial consistency rather than absolute classification accuracy. Future work should include field-based validation (e.g., through *in situ* surveys or underwater observations) to provide an independent and more robust assessment of classification performance.

In addition, the bathymetric model used for water column correction was derived from digitized nautical charts and interpolated to a spatial resolution of 10 m, which may limit the precision of the depth correction. Environmental factors such as water turbidity and light attenuation also influence the detectability of deeper portions of the meadows in optical satellite imagery.

Overall, the findings highlight the strong potential of integrating very high-resolution satellite imagery with object-based image analysis for the mapping and monitoring of PO habitats. The methodology presented in this study provides a robust framework that can support future monitoring efforts and can be further improved through the integration of higher-resolution bathymetric datasets, field observations, and comparisons with additional classification algorithms. Furthermore, while very high-resolution imagery provides significant advantages in terms of spatial detail and classification accuracy, it is associated with relatively high acquisition costs, which may limit its accessibility. In the case of the images used in this study, the cost is approximately 22.5$ per km^2 (apollomapping.com/pleiades-neo-satellite). This figure is only a rough estimate, as the actual price varies depending on factors such as whether the buyer requests a new acquisition or an existing archive image, the intended use of the data, and the buyer's institutional affiliation. In contrast, freely available medium-resolution datasets (e.g., Sentinel-2) offer a cost-effective alternative for large-scale or long-term monitoring, with the limitations of reduced spatial detail and potentially lower classification performance for fine-scale habitats such as PO meadows.

Acknowledgements

The authors would like to thank Airbus DS, Sysdeco S.r.l. and Dr. Fabrizio Filiberti for their assistance and generous provision of the images Pleaides NEO © Airbus DS (acquired in year 2021, 2022) used in this study.

References

Alcaras, E., Amoroso, P.P., Baiocchi, V., Falchi, U., Parente, C., 2021: Unsupervised classification based approach for coastline extraction from Sentinel-2 imagery. *Int. Workshop Metrol. Sea (MetroSea)*, 423–427. https://doi.org/10.1109/MetroSea52177.2021.9611583

Baiocchi, V., Bosman, A., Cianfanelli, F., Magurano, C., 2025. Neo-Pleiades imagery for Posidonia oceanica mapping. *2025 IEEE International Workshop on Metrology for Aerospace Metroaerospace 2025*, pp. 828–832. https://doi.org/10.1109/MetroAeroSpace64938.2025.11114417

Boser, B.E., Guyon, I.M., Vapnik, V.N., 1992: A training algorithm for optimal margin classifiers. Proceedings of the Fifth Annual Workshop on Computational Learning Theory, 144–152.

Cammarano, F., Roisenberg, H.B., Conclave, A., Fadel, I., van der Meijde, M., 2025: On the crustal composition of the Sardinia–Corsica continental block inferred from receiver functions. *Solid Earth*, 16(2), 135–154. https://doi.org/10.5194/se-16-135-2025

Chowdhury, M., Martínez-Sansigre, A., Mole, M., Alonso-Peleato, E., Basos, N., Blanco, J.M., Ramirez-Nicolas, M., Caballero, I., de la Calle Perez, I., 2024: AI-driven remote sensing enhances Mediterranean seagrass monitoring and conservation to combat climate change and anthropogenic impacts. *Sci. Rep.*, 14. https://doi.org/10.1038/s41598-024-59091-7

Cocozza di Montanara, A., Semprucci, F., Rendina, F., Russo, G.F., Sandulli, R., 2024: Re-discovering macerating *Posidonia oceanica* bottoms: Characterization of meiofaunal community inhabiting a peculiar Mediterranean habitat. *Estuar. Coast. Shelf Sci.*, 309, 108956. https://doi.org/10.1016/j.ecss.2024.108956

Giménez-Romero, À., Ferchichi, D., Moreno-Spiegelberg, P., Sintes, T., Matías, M.A., 2025: A generalizable deep learning framework for large-scale mapping of seagrass habitats. *Ecological Indicators*, 180, 114349. https://doi.org/10.1016/j.ecolind.2025.114349

Lyzenga, D.R., 1978. Passive remote sensing techniques for mapping water depth and bottom features. Applied Optics, 17, 379–383. https://doi.org/10.1364/AO.17.000379

Makri, D., Christofilakos, S., Poursanidis, D., Traganos, D., Mettas, C., Stylianou, N., Hadjimitsis, D., 2025: Seagrass mapping in Cyprus using Earth observation advances. Remote Sensing, 17, 3610. https://doi.org/10.3390/rs17213610

Panagou, T., Oikonomou, E., Hasiotis, T., Velegrakis, A.F., 2020: Shallow water bathymetry derived from green wavelength terrestrial laser scanner. *Mar. Geodesy*, 43, 472–492. https://doi.org/10.1080/01490419.2020.1737602

Rende, S.F., Bosman, A., Di Mento, R., Bruno, F., Lagudi, A., Irving, A.D., Dattola, L., Giambattista, L.D., Lanera, P., Proietti, R., et al., 2020. Ultra-high-resolution mapping of *Posidonia oceanica* (L.) Delile meadows through acoustic, optical data and object-based image classification. *J. Mar. Sci. Eng.*, 8, 647. https://doi.org/10.3390/jmse8090647

Rende, S.F., Bosman, A., Menna, F., Lagudi, A., Bruno, F., Severino, U., Montefalcone, M., Irving, A.D., Raimondi, V., Calvo, S., Pergent, G., Pergent-Martini, C., Tomasello, A., 2022. Assessing seagrass restoration actions through a micro-bathymetry survey approach (Italy, Mediterranean Sea). *Water*, 14(8), 1285. https://doi.org/10.3390/w14081285

Robello, C., Acunto, S., Leone, L.M., Mancini, I., Oprandi, A., Montefalcone, M., 2024: Large-scale re-implantation efforts for *Posidonia oceanica* restoration in the Ligurian Sea: Progress and challenges. *Diversity*, 16, 226. https://doi.org/10.3390/d16040226

Roca, M., Lee, C.B., Pertiwi, A.P., Blume, A., Caballero, I., Navarro, G., Traganos, D., 2025: Subtidal seagrass and blue carbon mapping at the regional scale: a cloud-native multi-temporal Earth observation approach. *GISci. Remote Sens.*, 62, 1. https://doi.org/10.1080/15481603.2024.2438838

Traganos, D., Lee, C.B., Blume, A., Poursanidis, D., Čižmek, H., Deter, J., Mačić, V., Montefalcone, M., Pergent, G., Pergent-Martini, C., Ricart, A.M., Reinartz, P., 2022: Spatially explicit seagrass extent mapping across the entire Mediterranean. Front. Mar. Sci., 9, 871799. https://doi.org/10.3389/fmars.2022.871799

Trevathan-Tackett, S.M., Kelleway, J., Macreadie, P.I., Beardall, J., Ralph, P., Bellgrove, A., 2015: Comparison of marine macrophytes for their contributions to blue carbon sequestration. *Ecology*, 96, 3043–3057. https://doi.org/10.1890/15-0149.1

Ventura, D., Bonifazi, A., Gravina, M.F., Belluscio, A., Ardizzone, G., 2018: Mapping and classification of ecologically sensitive marine habitats using unmanned aerial vehicle (UAV) imagery and Object-Based Image Analysis (OBIA). *Remote Sensing*, 10(9), 1–23. https://doi.org/10.3390/rs10091331

Yfantidou, A., Hadjimitsis, D., 2019: Comparison of classification algorithms on optical satellite imagery for mapping *Posidonia oceanica* meadows: The case study of Limassol, Cyprus. *Remote Sensing of Clouds and the Atmosphere XXI*, 11150, 111500Q. https://doi.org/10.1117/12.2533462

Zaaboub, N., Guebsi, R., Chaouachi, R.S., Brik, B., Rotini, A., Chiesa, S., Rende, S.F., Makhloufi, M., Hamza, A., Galgani, F., El Bour, M., 2023: Using unmanned aerial vehicles (UAVs) and machine learning techniques for the assessment of *Posidonia* debris and marine (plastic) litter on coastal ecosystems. *Reg. Stud. Mar. Sci.*, 67, 103185. https://doi.org/10.1016/j.rsma.2023.103185

https://apollomapping.com/pleiades-neo-satellite (last accessed on: March 25th 2026)

https://www.garmin.com/it-IT/c/marine-cartography/third-party-marine-maps/ (last accessed on: March 25th 2026)